Extreme Mechanics Letters 51 (2022) 101594

Contents lists available at ScienceDirect

Extreme Mechanics Letters

journal homepage: www.elsevier.com/locate/eml

A network-based visco-hyperelastic constitutive model for optically clear adhesives

Tiankai Zhao [a,*], Jinrui Cao [a], Xin Li [a], Mingyong Xia [b], Bing Xue [b,*], Hongyan Yuan [a,*]

[a] Department of Mechanics and Aerospace Engineering, Southern University of Science and Technology, Shenzhen, Guangdong 518055, China
[b] Guangdong OPPO Mobile Telecommunications Corp., Ltd., Dongguan, Guangdong 523860, China

ARTICLE INFO

Article history:
Received 21 October 2021
Received in revised form 9 December 2021
Accepted 15 December 2021
Available online 24 December 2021

Keywords:
Visco-hyperelasticity
Full-network model
Entanglement
Free chains
Optically clear adhesives
ABAQUS UMAT

ABSTRACT

Optically clear adhesives (OCAs) are widely used as bonding materials in display industries. Accurate characterizations on the mechanical behaviors of OCAs are fundamental inputs in bending stress analysis of foldable displays for the optimal design purpose. Yet only a few works have studied the mechanical behaviors of OCAs. No network-based visco-hyperelastic constitutive model has ever been developed or applied to OCAs. In this work, we propose a visco-hyperelastic constitutive model based on the microscopic structure of polymer networks to characterize the mechanical behaviors of OCAs under different loading conditions. The model considers that the OCA consists of crosslinked networks and free chains, both of which are under topological constraints induced by entanglements. The hyperelastic response comes from the crosslinked networks, while the viscoelastic response originates from the free chains. We test the OCAs produced by 3M by loading them to large deformations with different loading rates. Results show that our model can well capture the visco-hyperelastic mechanical behaviors under these conditions. In addition, we program our constitutive model into ABAQUS UMAT and use two case studies to show the application of our model in finite element simulations.

1. Introduction

Optically clear adhesive (OCA), a kind of soft, transparent, and nearly incompressible elastomer, is widely used as bonding materials in foldable displays like flexible organic light-emitting diode (OLED) and active-matrix organic light-emitting diode (AMOLED) screens because of its good adhesion [1]. As a product of acrylate chemistry, OCAs consist of crosslinked networks and free chains, [2–5] and hence have a rate-dependent visco-hyperelastic behavior under mechanical loadings [6]. An accurate characterization on such mechanical properties is vital to the bending stress analysis in the next-generation foldable displays since it serves as the fundamental study for the optimal design purpose [7].

Quiet a lot of hyperelastic constitutive models have been developed for soft polymers, most of which are phenomenological [8–12]. In order to characterize the mechanical behaviors of such materials by a desired accuracy, some network-based constitutive models have been developed by looking into the microscopic structures of the polymers. Based on statistical mechanics, two models, the Gaussian chain model and the non-Gaussian chain model, have been developed to characterize the conformation of polymer chains under deformation [13]. The former one assumes a Gaussian probability distribution of the polymer chain density under a given stretch [14]. The latter one adopts the Kuhn–Grün probability distribution function to describe the statistical distribution of the chain density under finite extensibility [15]. It is found that for large deformations, the Kuhn–Grün model is much more accurate [15]. The work then focuses on how to model the network of a great deal of polymer chains and bridge the gap between the microscopic structures and the macroscopic properties to obtain a continuum theory that can characterize the mechanical response of soft polymers under finite deformations. A lot of models have been proposed afterwards, including James–Guth-three-chain-model [16], Arruda–Boyce-eight-chain-model [17], the average-stretch-model [18], and Wu–Giessen full-network model [19], all assuming an affine deformation of the polymer networks. Later on, Miehe et al. [20] proposed a micro–macro approach to rubber-like materials based on the non-affine micro-sphere model. Another important feature of the microstructure of polymers is the topological constraint effects owing to the entanglement of polymer chains [21]. To capture this effect, Deam and Edwards [22], Edwards and Vilgis [23], Doi and Edwards [24,25], Heinrich and Straube [26,27], Heinrich and Kaliske [28], and Heinrich et al. [29] developed the so-called tube model. The theory basically says the polymer chain is constrained in a virtual tube whose diameter is determined by the macroscopic deformation of the polymer [25]. Meissner and

* Corresponding authors.
E-mail addresses: zhaotk@sustech.edu.cn (T. Zhao), xuebing1@oppo.com (B. Xue), yuanhy3@sustech.edu.cn (H. Yuan).

https://doi.org/10.1016/j.eml.2021.101594
2352-4316/

Matějka [30], Miehe et al. [20], and Xiang et al. [31], combined the tube model with the eight-chain model, the non-affine micro-sphere model, and the average-stretch model, respectively, to characterize the hyperelasticity of soft polymers.

The finite deformation viscoelastic models have also been extensively studied. Simo and Holzapfel propose their viscoelastic models based on the evolutions of the internal variables, along with the material update schemes for finite element implementations [32,33]. Based on their efforts, Lion [34], and Reese and Govindjee [35] developed new constitutive models by different evolution equations of internal variables to address the characterization on hysteresis. Bergström and Boyce [36] formulated a nonlinear evolution law on internal variables for their viscoelastic model by making an emphasis on the study of the hysteresis of biological tissues. Miehe and Göktepe [37] developed a viscoelastic model with the non-affine effect of deformation based on their previous work [20]. Recently, Khajehsaeid et al.'s work [38] studied a new viscoelastic model by combining the hereditary integral with a strain-rate-dependent relaxation time scale. Liu et al. [39] developed a finite deformation linear model for viscoelastodynamics based on a thermodynamically consistent evolution equation of viscoelastic internal variables. Besides these phenomenological models, several network-based viscoelastic models have also been proposed. Doi and Edwards [25,40] pointed out that the viscoelasticity of polymers consists of two processes: the contour length relaxation process and the disengagement process of the primitive chain. The relaxation functions and the associated viscous parameters have been formulated and calculated respectively in subsequent works [40,41]. Based on these studies, Xiang et al. [42] proposed a network-based visco-hyperelastic model on soft digital materials (DMs). Clifton et al. [43] proposed a network-based, quasilinear viscoelastic model for polyurea. Tang et al. [44] worked out a two-scale mechanism-based theory of nonlinear viscoelasticity by an improvement of the tube model to describe the free chain motion at microscales. Besides these continuum models, molecular dynamics and multiscale simulations also play a role in modeling viscoelasticity of elastomers. Li et al. [45] applied coarse-grained model to acquire the tube diameter and primitive chain length of the entangled network and used these results as the input of the continuum level computations. Later, Li et al. [46] adopted the large-scale molecular dynamics to reveal some important physical mechanisms of crosslinked network and free chains.

For OCAs used in flexible displays, several phenomenological models have been applied to study their mechanical behaviors. For instance, Cheng et al. [47] adopted some phenomenological hyperelastic models to characterize the mechanical behavior of OCA and apply them on a bending simulation of AMOLED display. Salmon et al. [48] adopted a linear viscoelastic model to characterize the OCA used in a foldable display panel. Jia et al. [7] and Nath and Gupta [49] used Yeoh model associated with Simo's viscoelastic theory to characterize the mechanical behaviors of OCAs. Yet such characterizations are restricted in a relatively small deformation range (stretch $\leq$ 3) without any depiction on the rate-dependent stress behavior. And no network-based visco-hyperelastic constitutive model has ever been applied to this material.

In the present paper, we propose a three-dimensional network-based visco-hyperelastic model for OCAs. This model considers both Wu and Giessen's full-network polymer structures [19] and free polymer chains along with topological constraints. Two main origins of viscoelasticity: the contour length relaxation and the disentanglement of free chains are taken into consideration. The micro-sphere integral used in the model is calculated numerically with a great accuracy and speed. The viscoelastic stress is updated with respect to time in a recursion manner. The model is validated by the experimental tests conducted on 3M OCAs. The rate-dependent mechanical response of the model is thoroughly studied in the paper. A material update scheme is developed for the numerical implementation of our constitutive model.

The paper is arranged in the following way. In Section 2, we describe the derivation of the network-based visco-hyperelastic constitutive model and propose a material update scheme for the finite element method. In Section 3, the experimental setup is briefly described. In Section 4, the experimental data are applied to validate our constitutive model under different loading conditions. We also compare the full-network chain model with other two simplified-network models. Then, we present two case studies by using an ABAOUS UMAT subroutine where our constitutive model is programmed. We summarize our work in Section 5.

2. The constitutive model

The OCAs used as display bondings are products of acrylate chemistry. Just like other soft polymer compounds, the molecular network of OCA consists of crosslinked network and free chains, which are usually made of methyl methacrylate (MMA) or 2-hydroxyethyl acrylate (HEA) monomers [50]. In the rubbery state, the stress in such material is contributed by two parts: one is the hyperelastic part from the crosslinked network (Fig. 1(a)), the other is the viscoelastic part from the free chains (Fig. 1(b)) [42]. Both the crosslinked network and free chains are under topological constraints which are arising from entanglements. The polymer chains can only move and deform under such constraints depicted by the tube model (Fig. 1(a2) & (b2)).

2.1. The hyperelasticity of soft polymers

The crosslinked networks are the main contribution to the hyperelasticity of the polymer since they achieve the equilibrium under applied loads at instant. The deformation of a single polymer chain is characterized by entropic elasticity. That is, the force within a polymer chain is determined by its possible microstate which is characterized by the end-to-end stretch (Fig. 1(a1)). Most of the polymer chains in the network can only move and deform under the constraints of the surrounding chains due to entanglement [24]. A so-called tube model is proposed to characterize such constraints applied on these polymer chains [24,25]. Generally speaking, the move and the deformation of the polymer chains are constrained within a tube of a uniform diameter d which depends on the macroscopic deformation of the material. With this constraint, the primitive path (the shortest end-to-end path of a single polymer chain with the same topology as the chain itself) of each polymer chain cannot intersect with each other. As the tube deforms with the entire piece of the material, the polymer chain takes random walks within the tube and the contour length of the primitive path fluctuates, creating additional microstates. Hence, an extra entropy arises to the whole crosslinked network. By using an additive split, the Helmholtz free energy density of an individual chain in the crosslinked networks can be written into two parts:

$$W = W^f + W^c, \tag{1}$$

where W^f is the free energy of the end-to-end deformation of the polymer chain; while W^c characterizes the free energy of the fluctuation in the contour length of the polymer chain because of entanglement. The Helmholtz free energy in Eq. (1) can be written in the form of the probability density functions: ψ^f and ψ^c that describe the possible microstates of the end-to-end deformation and the fluctuated contour length given by the tube-like constraint, respectively:

$$W = -k_B T(\ln \psi^f + \ln \psi^c), \tag{2}$$

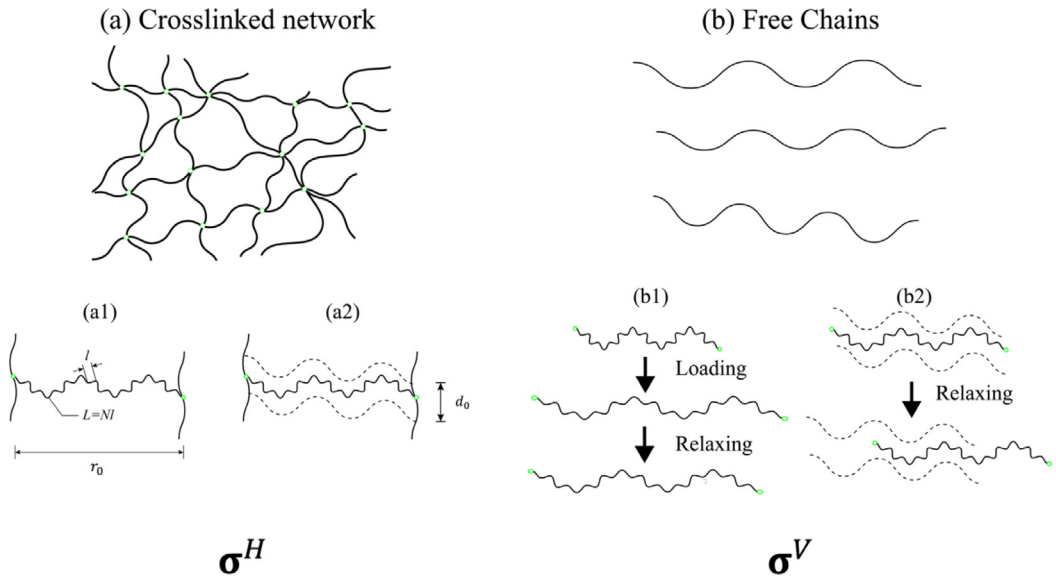

Fig. 1. The OCA is decomposed into the (a) crosslinked network and (b) free chains. The total stress is split into two parts: the hyperelastic part $\boldsymbol{\sigma}^H$, and the viscous part $\boldsymbol{\sigma}^V$. The hyperelastic part $\boldsymbol{\sigma}^H$ is a composition of (a1) the end-to-end conformation of the network chain and (a2) the tube-like topological constraint. The viscous part $\boldsymbol{\sigma}^V$ arises from two relaxation processes: (b1) the contour length relaxation of free chains and (b2) the disentanglement process of free chains modeled by reptations in tube-like constraints.

where k_B is Boltzmann constant and T is the temperature. Next, we will look for the approach to write out the explicit expressions for both ψ^f and ψ^c. In polymer science, the geometric structure of a polymer chain is idealized to be composed by averagely N segments called monomers with an equal length of l. For an unstrained free chain, the end-to-end distance r_0 can be obtained by statistical mechanics: $r_0 = \sqrt{N}l$ (Fig. 1(a1)) [18]. By adopting r to be the current deformed end-to-end distance as the polymer chain is strained, one can derive the stretch λ and the relative stretch λ_r respectively:

$$\lambda = \frac{r}{r_0} \text{ and } \lambda_r = \frac{r}{Nl} = \frac{\lambda}{\sqrt{N}}, \tag{3}$$

with $\lambda \in [0, \sqrt{N})$ and $\lambda_r \in [0, 1)$. For polymer chains under finite extensibility, the probability density of a single polymer chain is a function on the relative stretch that obeys Langevin probability distribution:

$$\psi^f = \psi_0^f \exp[-\lambda_r N L^{-1}(\lambda_r) - N \ln \frac{L^{-1}(\lambda_r)}{\sinh L^{-1}(\lambda_r)}], \tag{4}$$

where ψ_0^f is the normalizing coefficient; $L^{-1}(\cdot)$ is the inverse Langevin function. Therefore, the contribution to the free energy of the deformation of the polymer chain without entanglement can be written as:

$$W^f = k_B T \left[\lambda_r N L^{-1}(\lambda_r) + N \ln \frac{L^{-1}(\lambda_r)}{\sinh L^{-1}(\lambda_r)}\right] + W_0^f, \tag{5}$$

where $W_0^f = k_B T \ln \psi_0^f$ is a constant. Next, we consider the free energy arising from the tube-like constraint due to entanglement. According to Doi and Edwards's hypothesis [25], by taking the polymer chain as a random reptation confined within a tube, its fluctuated contour length given by the tube-like constraint leads to the probability density function:

$$\psi^c = \psi_0^c \exp[-\alpha \left(\frac{r_0}{d}\right)^2], \tag{6}$$

where ψ_0^c is the normalizing coefficient; α is a factor that depends on the shape of the cross-section of the tube. Henrich and Straube [26,27] proposed a relationship between the deformation-dependent tube diameter d and the principal stretch λ_i:

$$d_i = d_0 \lambda_i^{1/2}, \tag{7}$$

where d_0 stands for the diameter of the undeformed tube (Fig. 1(a2)), while d_i denotes for the effective diameter of the deformed tube in the ith direction. One should notice that the tube diameter deforms nonaffinely in Eq. (7). According to Rubistein and Panyukov [51], it satisfies the condition of topological invariance under network deformation. And there are also other more generalized models from literatures that describe the nonaffine tube deformation in highly entangled networks [52–54]. Here we just adopt the one derived by Doi and Edwards [25] for simplicity. Combining Eqs. (6) and (7), ψ^c is then rewritten as:

$$\psi^c = (\psi_0^c)^3 \prod_{i=1}^{3} \exp[-\left(\frac{r_0}{d_0}\right)^2 \frac{\alpha}{\lambda_i}]. \tag{8}$$

The free energy from the entanglements of the tube-like constraints is:

$$W^c = \alpha k_B T N \frac{l^2}{d_0^2} \sum_{i=1}^{3} \frac{1}{\lambda_i} + W_0^c, \tag{9}$$

where $W_0^c = 3k_B T \ln \psi_0^c$. By letting $G^e = \alpha k_B T N \frac{l^2}{d_0^2}$, W^c can be rewritten as:

$$W^c = G^e \sum_{i=1}^{3} \frac{1}{\lambda_i} + W_0^c. \tag{10}$$

For now, we have formulated the free energy of a single polymer chain in the crosslinked network. To relate this single-chain free energy with the macroscopic bulk energy of the polymer, we consider a unit sphere containing n polymer chains in the reference configuration. By assuming that all the chains are homogeneous, the free energy within the unit sphere is:

$$\boldsymbol{W} = \int_0^{\pi} \int_0^{2\pi} n(W^f + W^c) C \sin\theta \, \mathrm{d}\varphi \mathrm{d}\theta, \tag{11}$$

where θ and φ are the angular coordinates of the unit sphere in the reference configuration; C is the so-called molecular chain

orientation distribution function (CODF), named by Wu and Giessen [19]. We here briefly summarize the work described in their paper and follow their process to derive the constitutive law for the hyperelastic part of the stress. By noticing that the total number of the polymer chains conserves in the unit sphere and invoking the isotropic distribution, one can get C equals to $\frac{1}{4\pi}$ in the reference configuration. Unlike the tube constraint, we link the deformation of the single polymer chain to the macroscopic deformation of the polymer by adopting the affine deformation assumption:

$$\mathbf{r} = \mathbf{F}\mathbf{r}_0, \tag{12}$$

where $\mathbf{r}$ and $\mathbf{r}_0$ are the current and initial end-to-end vector of the polymer chain, respectively; $\mathbf{F}$ is the macroscopic deformation gradient. The initial end-to-end vector $\mathbf{r}_0$ can be parametrized in the spherical coordinate system as:

$$\mathbf{r}_0 = r_0(\sin\theta\cos\varphi\mathbf{e}_1 + \sin\theta\sin\varphi\mathbf{e}_2 + \cos\theta\mathbf{e}_3), \tag{13}$$

where $r_0 = |\mathbf{r}_0|$; $\{\mathbf{e}_i\}$ is a set of orthonormal basis defined in the reference configuration. The stretch λ then can be written as $\lambda^2 = \mathbf{r}_0 \cdot \mathbf{F}^{\mathrm{T}}\mathbf{F}\mathbf{r}_0/r_0^2$. By noticing that $\mathbf{F}^{\mathrm{T}}\mathbf{F}\mathbf{m}_i = \lambda_i^2 \mathrm{m}_i$ in an affine manner [19], with λ_i being the ith principal stretch, one can obtain:

$$\lambda^2 = \sum_{i=1}^{3} m_i^2\lambda_i^2, \tag{14}$$

where $m_1 = \sin\theta\cos\varphi$, $m_2 = \sin\theta\sin\varphi$, and $m_3 = \cos\theta$; $\mathbf{m}_i = \mathrm{m}_i\mathbf{e}_i$(no sum). The hyperelastic principal stress in the current configuration can then be written as:

$$\sigma_i^H = \lambda_i\frac{\partial \boldsymbol{W}}{\partial\lambda_i} - p, \text{(no sum on } i) \tag{15}$$

where p is the pressure term for the incompressible material. Substituting Eqs. (5), (10), and (11) into Eq. (15), we can derive the hyperelastic part of the principal stress by ignoring the term irrelevant to the deformation in the free energy function:

$$\sigma_i^H = \frac{1}{4\pi}C^R\sqrt{N}\int_0^{\pi}\int_0^{2\pi} L^{-1}\left(\frac{\lambda}{\sqrt{N}}\right)\frac{\lambda_i^2\,(m_i)^2}{\lambda}\sin\theta\mathrm{d}\theta\mathrm{d}\varphi - G^e/\lambda_i - p, \tag{16}$$

where the rubber modulus C^R=nk_BT. One should notice that the integral in Eq. (16) is performed in the reference configuration. The corresponding Cauchy stress tensor can be written as:

$$\boldsymbol{\sigma}^H = \sum_{i=1}^{3}\sigma_i^H\mathbf{n}_i\otimes\mathbf{n}_i, \tag{17}$$

where $\mathbf{n}_i$ is the ith principal direction of the left Cauchy–Green tensor. The integral is computed numerically by the method proposed of Miehe et al. [20] with a great accuracy and speed.

2.2. The viscoelasticity of soft polymers

Besides the crosslinked networks, soft polymers also contain free chains. Just like the crosslinked polymer chains, the free chains consist of a number of monomers and are entangled with their neighboring chains. Yet unlike the crosslinked chains, these free chains go to their thermal equilibrium at an observable time scale, thus, they contribute to the viscoelasticity of the polymers. The viscoelasticity mainly comes from two processes: one is the relaxation process of the end-to-end contour length of the primitive paths of free chains (Fig. 1(b1)); the other is the disentanglement process of free chains, modeled by reptation dynamics under the tube-like constraints (Fig. 1(b2)) [40]. Therefore, the viscous stress $\boldsymbol{\sigma}^V$ can be split into two parts, which are $\boldsymbol{\sigma}_f^V$ and $\boldsymbol{\sigma}_c^V$ with respect to two different relaxation functions φ_f and φ_c [42]. Based on previous works [38,42,55,56], one can express both parts of the viscous stress in the form of the convolution integral:

$$\boldsymbol{\sigma}_f^V(t) = \int_{-\infty}^{t}\frac{\partial\boldsymbol{\sigma}_f^H}{\partial\tau}\varphi_f(t-\tau)\,\mathrm{d}\tau = \boldsymbol{\sigma}_f^H(t) - \int_{-\infty}^{t}\boldsymbol{\sigma}_f^H(\tau)\frac{\partial\varphi_f(t-\tau)}{\partial\tau}\mathrm{d}\tau, \tag{18a}$$

$$\boldsymbol{\sigma}_c^V(t) = \int_{-\infty}^{t}\frac{\partial\boldsymbol{\sigma}_c^H}{\partial\tau}\varphi_c(t-\tau)\,\mathrm{d}\tau = \boldsymbol{\sigma}_c^H(t) - \int_{-\infty}^{t}\boldsymbol{\sigma}_c^H(\tau)\frac{\partial\varphi_c(t-\tau)}{\partial\tau}\mathrm{d}\tau, \tag{18b}$$

where $\boldsymbol{\sigma}_f^H$ and $\boldsymbol{\sigma}_c^H$ are the associated hyperelastic stress with respect to $\boldsymbol{\sigma}_f^V$ and $\boldsymbol{\sigma}_c^V$. One should notice that we have adopted the assumption: $\boldsymbol{\sigma}_f^V(t=-\infty) = \boldsymbol{\sigma}_c^V(t=-\infty) = 0$. The free chains can form transient crosslinked networks without preferred orientations due to twisting and knotting; [57] and their disentanglement process also involves fluctuation of the contour length under tube-like constraints. Hence, the associated hyperelastic stress of free chains can be assumed to have the same expressions with those of the crosslinked networks [42]. Here, we split the expressions of the hyperelastic stress into two parts and assign them new material parameters that characterize the mechanical properties of the free chains: the first part $\boldsymbol{\sigma}_f^H$ is contributed by the end-to-end deformation of a free chain, and the second part $\boldsymbol{\sigma}_c^H$ is contributed from the contour length fluctuation given by the tube-like constraint during disentanglement:

$$\boldsymbol{\sigma}_f^H = \sum_{i=1}^{3}\frac{1}{4\pi}C_V^R\sqrt{N_V}\int_0^{\pi}\int_0^{2\pi} L^{-1}\left(\frac{\lambda}{\sqrt{N_V}}\right) \times \frac{\lambda_i^2\left(m_i^0\right)^2}{\lambda}\sin\theta\mathrm{d}\theta\mathrm{d}\varphi\mathbf{n}_i\otimes\mathbf{n}_i - p_f\mathbf{I}, \tag{19a}$$

$$\boldsymbol{\sigma}_c^H = \sum_{i=1}^{3} -(G_V^e/\lambda_i)\mathbf{n}_i\otimes\mathbf{n}_i - p_c\mathbf{I}, \tag{19b}$$

where $\mathbf{I}$ is the second-order identity; C_V^R, N_V, and G_V^e are additional material parameters that need to be fitted, and usually are referred as material parameters of the free chains. The viscous stress $\boldsymbol{\sigma}_f^V$ originated from the contour length relaxation process will relax over a time scale τ_R. The stress $\boldsymbol{\sigma}_c^V$ arising from the disentanglement process, however, will relax over a different time scale τ_D. The relaxation functions, formulated by Lin [41], and Doi and Edwards [25], should be:

$$\varphi_f(t) = \sum_{k=odd}\frac{8}{k^2\pi^2}\exp(-k^2\mathrm{t}/\tau_R), \tag{20a}$$

$$\varphi_c(t) = \sum_{p=odd}\frac{8}{p^2\pi^2}\exp(-p^2\mathrm{t}/\tau_D). \tag{20b}$$

By summing Eqs. (19a) and (19b) together, one can obtain the viscous stress:

$$\boldsymbol{\sigma}^V = \boldsymbol{\sigma}_f^V + \boldsymbol{\sigma}_c^V. \tag{21}$$

The total Cauchy stress is then written as:

$$\boldsymbol{\sigma} = \boldsymbol{\sigma}^H + \boldsymbol{\sigma}^V. \tag{22}$$

Table 1
Implementation of the visco-hyperelastic constitutive model at the $t = t_{n+1}$ based on the results of $t = t_n$.

1	Calculate the hyperelastic part of the stress based on Eqs. (16) & (17) when $t = t_{n+1}$ $\sigma_i^H = \frac{1}{4\pi} C^R \sqrt{N} \int_0^{\pi} \int_0^{2\pi} L^{-1}\left(\frac{\lambda}{\sqrt{N}}\right) \frac{\lambda_i^2 \left(m_i^0\right)^2}{\lambda} \sin\theta \mathrm{d}\theta \mathrm{d}\varphi - G^e/\lambda_i - p$ $\boldsymbol{\sigma}^H = \sum_{i=1}^{3} \sigma_i^H \mathbf{n}_i \otimes \mathbf{n}_i$.
2	Calculate the viscous stress based on Eq. (29) when $t = t_{n+1}$ $\mathbf{h}_k^f(t_{n+1}) = \mathbf{q}_k^f(t_n) + \frac{8}{k^2\pi^2} \exp\left(-\frac{k^2\Delta t}{2\tau_R}\right) \left(\boldsymbol{\sigma}_f^H\right)_{n+1}$, $\mathbf{q}_k^f(t_{n+1}) = \exp\left(-\frac{k^2\Delta t}{2\tau_R}\right) [\exp\left(-\frac{k^2\Delta t}{2\tau_R}\right) \mathbf{h}_k^f(t_{n+1}) - \frac{8}{k^2\pi^2} \left(\boldsymbol{\sigma}_f^H\right)_{n+1}]$, $(\boldsymbol{\sigma}_f^V)_{n+1} = \sum_{k=odd} \mathbf{h}_k^f(t_{n+1})$.
3	Calculate the viscous stress based on Eq. (29) when $t = t_{n+1}$ $\mathbf{h}_p^c(t_{n+1}) = \mathbf{q}_p^c(t_n) + \frac{8}{p^2\pi^2} \exp\left(-\frac{p^2\Delta t}{2\tau_D}\right) \left(\boldsymbol{\sigma}_c^H\right)_{n+1}$, $\mathbf{q}_p^c(t_{n+1}) = \exp\left(-\frac{p^2\Delta t}{2\tau_D}\right) [\exp\left(-\frac{p^2\Delta t}{2\tau_D}\right) \mathbf{h}_p^c(t_{n+1}) - \frac{8}{p^2\pi^2} \left(\boldsymbol{\sigma}_c^H\right)_{n+1}]$, $(\boldsymbol{\sigma}_c^V)_{n+1} = \sum_{p=odd} \mathbf{h}_p^c(t_{n+1})$.
4	Sum up the results obtained by step 1∼3 to get the total Cauchy stress tensor: $\boldsymbol{\sigma} = \boldsymbol{\sigma}^H + \boldsymbol{\sigma}_f^V + \boldsymbol{\sigma}_c^V$ at $t = t_{n+1}$.
5	Calculate the elasticity tensor for $\boldsymbol{\sigma}^H$, $\boldsymbol{\sigma}_f^V$, and $\boldsymbol{\sigma}_c^V$ at $t = t_{n+1}$ according to Eq. (31)∼(33).
6	Calculate the spatial elasticity tensor with respect to the Jaumann rate of the total Cauchy stress tensor $\boldsymbol{\sigma}$ at $t = t_{n+1}$ by Eq. (30):

2.3. Material update algorithm of the constitutive model

This section summarizes the key details on the numerical implementation of the constitutive model. An algorithm is proposed to update the total Cauchy stress and the spatial elasticity tensor with respect to each time step. Now suppose we have obtained the value of $\boldsymbol{\sigma}_f^V$ at the time step $t = t_n$, which is $(\boldsymbol{\sigma}_f^V)_n$. Then the value of $\boldsymbol{\sigma}_f^V$ at the time step $t = t_{n+1}$ can be written as:

$$(\boldsymbol{\sigma}_f^V)_{n+1} = \int_{-\infty}^{t_{n+1}} \frac{\partial \boldsymbol{\sigma}_f^H}{\partial \tau} \varphi_f(t_{n+1} - \tau) \mathrm{d}\tau. \tag{23}$$

Substituting Eq. (20a) into Eq. (23), one can have:

$$(\boldsymbol{\sigma}_f^V)_{n+1} = \int_{-\infty}^{t_{n+1}} \frac{\partial \boldsymbol{\sigma}_f^H}{\partial \tau} \sum_{k=odd} \frac{8}{k^2\pi^2} \exp[-\frac{k^2(t_{n+1} - \tau)}{\tau_R}] \mathrm{d}\tau, \tag{24}$$

By letting $\mathbf{h}_k^f(t_{n+1})$ denote for $\int_{-\infty}^{t_{n+1}} \frac{\partial \boldsymbol{\sigma}_f^H}{\partial \tau} \frac{8}{k^2\pi^2} \exp[-\frac{k^2(t_{n+1}-\tau)}{\tau_R}] \mathrm{d}\tau$, one can have:

$$(\boldsymbol{\sigma}_f^V)_{n+1} = \sum_{k=odd} \mathbf{h}_k^f(t_{n+1}). \tag{25}$$

Meanwhile, the time integral in Eq. (24) can be re-integrated with respect to the time intervals $\tau \in (-\infty, t_n]$ and $\tau \in (t_n, t_{n+1}]$; and

$$\begin{aligned}(\boldsymbol{\sigma}_f^V)_{n+1} = &\sum_{k=odd} \exp(-\frac{k^2\Delta t}{\tau_R}) \mathbf{h}_k^f(t_n) \\ &+ \int_{t_n}^{t_{n+1}} \frac{\partial \boldsymbol{\sigma}_f^H}{\partial \tau} \sum_{k=odd} \frac{8}{k^2\pi^2} \exp[-\frac{k^2(t_{n+1} - \tau)}{\tau_R}] \mathrm{d}\tau,\end{aligned} \tag{26}$$

where $\Delta t = t_{n+1} - t_n$. To numerically calculate the time integral in Eq. (26), we apply the means of the midpoint rule, i.e., $t \sim \frac{t_n + t_{n+1}}{2}$. The time derivative then becomes $\left.\frac{\partial \boldsymbol{\sigma}_f^H}{\partial \tau}\right|_{\frac{t_n+t_{n+1}}{2}} \approx \frac{\left(\boldsymbol{\sigma}_f^H\right)_{n+1} - \left(\boldsymbol{\sigma}_f^H\right)_n}{\Delta t}$, and the recursion law for $\mathbf{h}_k^f(t_n)$:

$$\mathbf{h}_k^f(t_{n+1}) = \exp(-\frac{k^2\Delta t}{\tau_R}) \mathbf{h}_k^f(t_n) + \frac{8}{k^2\pi^2} \exp\left(-\frac{k^2\Delta t}{2\tau_R}\right) [\left(\boldsymbol{\sigma}_f^H\right)_{n+1} - \left(\boldsymbol{\sigma}_f^H\right)_n]. \tag{27}$$

One can further let $\mathbf{q}_k^f(t_n) = \exp\left(-\frac{k^2\Delta t}{2\tau_R}\right) [\exp\left(-\frac{k^2\Delta t}{2\tau_R}\right) \mathbf{h}_k^f(t_n) - \frac{8}{k^2\pi^2} \left(\boldsymbol{\sigma}_f^H\right)_n]$, and get the stress update algorithm for $\boldsymbol{\sigma}_f^V$, that is:

$$\mathbf{h}_k^f(t_{n+1}) = \mathbf{q}_k^f(t_n) + \frac{8}{k^2\pi^2} \exp\left(-\frac{k^2\Delta t}{2\tau_R}\right) \left(\boldsymbol{\sigma}_f^H\right)_{n+1}, \tag{28a}$$

$$\begin{aligned}\mathbf{q}_k^f(t_{n+1}) = &\exp\left(-\frac{k^2\Delta t}{2\tau_R}\right) [\exp\left(-\frac{k^2\Delta t}{2\tau_R}\right) \mathbf{h}_k^f(t_{n+1}) \\ &- \frac{8}{k^2\pi^2} \left(\boldsymbol{\sigma}_f^H\right)_{n+1}],\end{aligned} \tag{28b}$$

$$(\boldsymbol{\sigma}_f^V)_{n+1} = \sum_{k=odd} \mathbf{h}_k^f(t_{n+1}). \tag{28c}$$

Similarly, the stress update algorithm for $\boldsymbol{\sigma}_c^V$ is:

$$\mathbf{h}_p^c(t_{n+1}) = \mathbf{q}_p^c(t_n) + \frac{8}{p^2\pi^2} \exp\left(-\frac{p^2\Delta t}{2\tau_D}\right) \left(\boldsymbol{\sigma}_c^H\right)_{n+1}, \tag{29a}$$

$$\begin{aligned}\mathbf{q}_p^c(t_{n+1}) = &\exp\left(-\frac{p^2\Delta t}{2\tau_D}\right) [\exp\left(-\frac{p^2\Delta t}{2\tau_D}\right) \mathbf{h}_p^c(t_{n+1}) \\ &- \frac{8}{p^2\pi^2} \left(\boldsymbol{\sigma}_c^H\right)_{n+1}],\end{aligned} \tag{29b}$$

$$(\boldsymbol{\sigma}_c^V)_{n+1} = \sum_{p=odd} \mathbf{h}_p^c(t_{n+1}). \tag{29c}$$

Combining Eqs. (21)∼(22), (28a)∼(28c), and (29a)∼(29c), we have the full scheme of the total Cauchy stress update algorithm which is summarized in Table 1.

The spatial elasticity tensor with respect to the Jaumann rate of the total Cauchy stress tensor $\boldsymbol{\sigma}$ at $t = t_{n+1}$ can be readily derived from Eqs. (22), (28a), and (29a), which is:

$$\begin{aligned}\mathbf{c}_{tot}(t_{n+1}) = &\mathbf{c}_0(t_{n+1}) + \sum_{k=odd} \frac{8}{k^2\pi^2} \exp\left(-\frac{k^2\Delta t}{2\tau_R}\right) \mathbf{c}_k^f(t_{n+1}) \\ &+ \sum_{p=odd} \frac{8}{p^2\pi^2} \exp\left(-\frac{p^2\Delta t}{2\tau_D}\right) \mathbf{c}_p^c(t_{n+1}) + \boldsymbol{\sigma} \otimes \mathbf{I} + \mathbf{I} \otimes \boldsymbol{\sigma},\end{aligned} \tag{30}$$

where $\mathbf{c}_0$ is the elasticity tensor with respect to $\boldsymbol{\sigma}^H$, $\mathbf{c}_k^f$ is the elasticity tensor with respect to $\boldsymbol{\sigma}_f^H$, and $\mathbf{c}_k^c$ is the elasticity tensor with respect to $\boldsymbol{\sigma}_c^H$. The way to calculate the spatial elasticity tensor $\mathbf{c}$ with respect to an elastic energy density function $\boldsymbol{W}$ of an incompressible elastomer can be found in the work by Connolly et al. [58]:

$$\begin{aligned}\mathbf{c} = &\sum_{a,b=1}^{3} (\gamma_{ab} - 2\delta_{ab}\beta_a)(\mathbf{n}_a \otimes \mathbf{n}_a \otimes \mathbf{n}_b \otimes \mathbf{n}_b) \\ &+ \sum_{a,b=1;a\neq b}^{3} \frac{\beta_b\lambda_a^2 - \beta_a\lambda_b^2}{\lambda_b^2 - \lambda_a^2} [(\mathbf{n}_a \otimes \mathbf{n}_b)(\mathbf{n}_a \otimes \mathbf{n}_b + \mathbf{n}_b \otimes \mathbf{n}_a)],\end{aligned} \tag{31}$$

where

$$\begin{aligned}\gamma_{ab} = &\left[\bar{\lambda}_b(\bar{\lambda}_a \frac{\partial \boldsymbol{W}}{\partial \bar{\lambda}_a}) \frac{\partial \boldsymbol{W}}{\partial \bar{\lambda}_b}\right] + \frac{1}{9} \sum_{c,d=1}^{3} [\bar{\lambda}_d(\bar{\lambda}_c \frac{\partial \boldsymbol{W}}{\partial \bar{\lambda}_c}) \frac{\partial \boldsymbol{W}}{\partial \bar{\lambda}_d}] \\ &- \frac{1}{3} \sum_{c=1}^{3} [\bar{\lambda}_c(\bar{\lambda}_a \frac{\partial \boldsymbol{W}}{\partial \bar{\lambda}_a}) \frac{\partial \boldsymbol{W}}{\partial \bar{\lambda}_c} + \bar{\lambda}_b(\bar{\lambda}_c \frac{\partial \boldsymbol{W}}{\partial \bar{\lambda}_c}) \frac{\partial \boldsymbol{W}}{\partial \bar{\lambda}_b}],\end{aligned} \tag{32}$$

$$\beta_a = \bar{\lambda}_a \frac{\partial \boldsymbol{W}}{\partial \bar{\lambda}_a} - \frac{1}{3} \sum_{b=1}^{3} \bar{\lambda}_b \frac{\partial \boldsymbol{W}}{\partial \bar{\lambda}_b}, \tag{33}$$

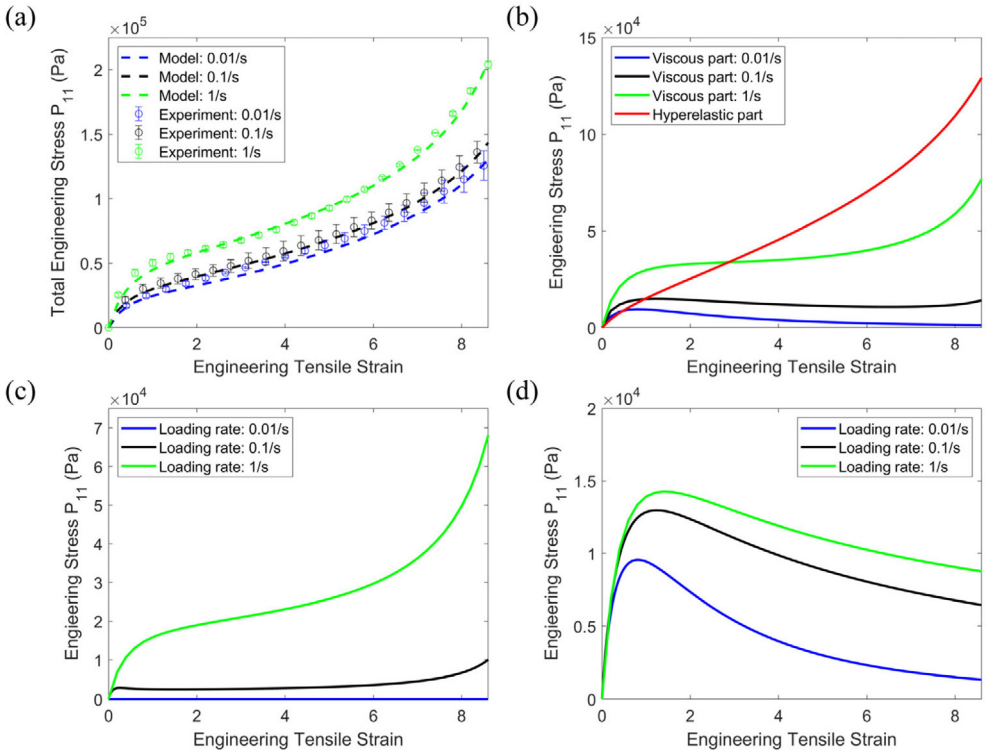

Fig. 2. The fitting results of engineering stress–strain curves for uniaxial tension. The engineering tensile strain is defined as the elongated length of the sample divided by the original length. The 11-component of the stress tensor is plotted. (a): the experimental data and fitting results of uniaxial tension test at stretch rates $\dot{\varepsilon} = 0.01\ s^{-1}$, $0.1\ s^{-1}$, and $1\ s^{-1}$; each loading rate is tested by multiple times and the standard deviations are plotted in error bars. (b): The hyperelastic part $\mathbf{P}^H$ and the viscous part $\mathbf{P}^V$ of the engineering stress for different loading rates. (c): the engineering stress $\mathbf{P}_f^V$ contributed from the contour length relaxation of free chains at different loading rates. (d): the engineering stress $\mathbf{P}_c^V$ contributed from the disentanglement of free chains at different loading rates.

For incompressible materials: $\overline{\lambda}_a = J^{-\frac{1}{3}}\lambda_a$. The derivations and other details of Eq. (31) ∼(33) are not included in this paper for simplicity.

3. The experimental setup

Uniaxial tension experiments on 3M optically clear adhesives (OCAs) are conducted on an Instron 6800 material testing machine at different stretch rates $\dot{\varepsilon} = 0.01\ s^{-1}$, $0.1\ s^{-1}$, and $1\ s^{-1}$. The applied deformation can be characterized by the following deformation gradient:

$$\mathbf{F}_{uni} = \begin{bmatrix} 1+\dot{\varepsilon}t & 0 & 0 \\ 0 & (1+\dot{\varepsilon}t)^{-1/2} & 0 \\ 0 & 0 & (1+\dot{\varepsilon}t)^{-1/2} \end{bmatrix}. \tag{34}$$

The experiments are carried out under the room temperature with a 50% relative humidity. The dimension of our material is 40 mm × 10 mm × 0.1 mm (Length × Width × Thickness). The loading speed of the testing machine is determined by the stretch rate $\dot{\varepsilon}$ and the length of the sample between the upper and the lower clamps. The displacement and the force are recorded by the testing machine.

We also conduct the simple shear test on a TA DMA850 dynamic thermoelastic analysis (DMA) machine at different loading rates $\dot{\varepsilon} = 0.01\ s^{-1}$, $0.1\ s^{-1}$, and $1\ s^{-1}$ for the same type of OCA. The applied deformation can be characterized by the following deformation gradient:

$$\mathbf{F}_{shear} = \begin{bmatrix} 1 & \dot{\varepsilon}t & 0 \\ 0 & 1 & 0 \\ 0 & 0 & 1 \end{bmatrix}. \tag{35}$$

The experiments are carried out under the room temperature with the same relative humidity. The dimension of the tested material is 10 mm × 10 mm × 0.1 mm (Length × Width × Thickness). The loading speed of the machine is determined by the stretch rates $\dot{\varepsilon}$ and the thickness of the sample.

The stress relaxation test and the loading–unloading test are conducted on the same DMA machine by using the simple shear mode. In the stress relaxation test, the samples are loaded up to 500% engineering shear strain at shear rates $\dot{\varepsilon} = 0.01\ s^{-1}$, and $0.1\ s^{-1}$, then are held steady for 900 s. In the loading–unloading test, the samples are loaded up to 800% engineering shear strain at shear rates $\dot{\varepsilon} = 0.01\ s^{-1}$, and $0.1\ s^{-1}$, then are unloaded to zero stress state with the unloading rate $\dot{\varepsilon} = -0.01\ s^{-1}$, and $-0.1\ s^{-1}$, respectively. The time–force curve is recorded by the DMA machine.

4. Results and discussions

In this part, we apply our constitutive model to fit the experimental data of the 3M OCAs. The material parameters are extracted by matching the constitutive model with results from the uniaxial tension test and the simple shear test. The relaxation test and the loading–unloading test are carried out to verify the fitting results. A comparison between the full-network model with other simplified-network models is presented afterwards. We then program the constitutive model into ABAQUS UMAT by using the algorithm proposed in Section 2.3. Two cases are shown as the examples that verify the applicability of our model to finite element simulations.

4.1. The fitting results under the room temperature

In this section, we apply the Nelder–Mead method [59] to fit the material parameters by using the experimental data derived from the uniaxial tension test (Fig. 2) and the simple shear test

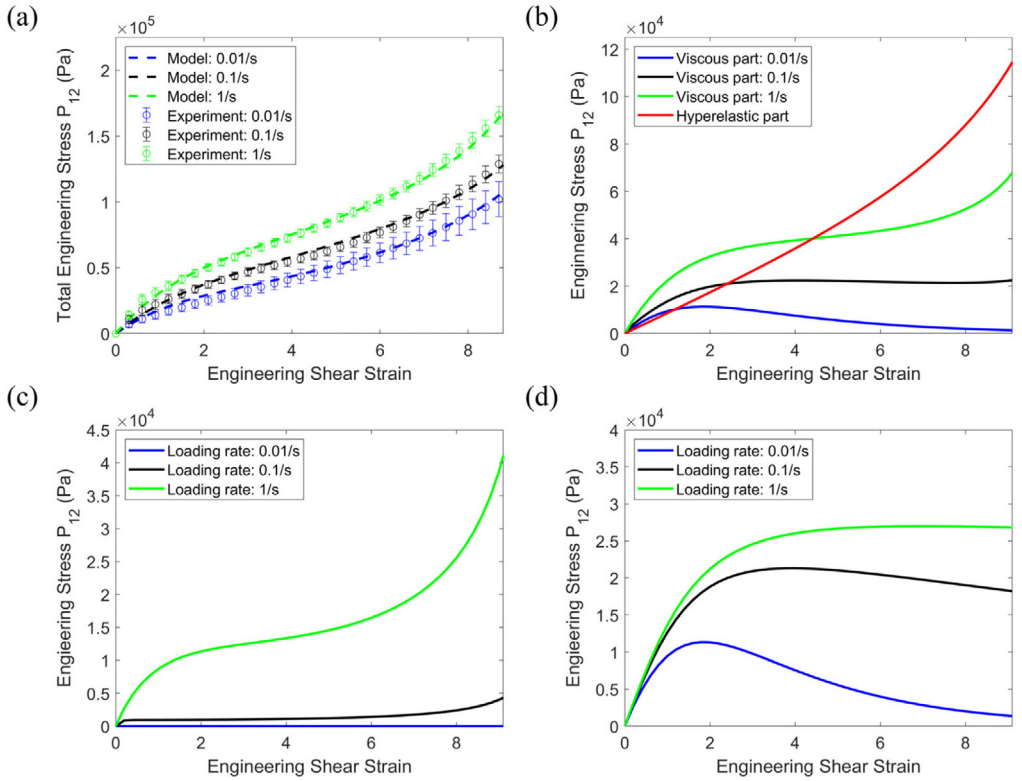

Fig. 3. The fitting results of engineering stress–strain curves for simple shear. The 12-component of the stress tensor is plotted. (a): the experimental data and fitting results of uniaxial tension test at stretch rates $\dot{\varepsilon} = 0.01\ \mathrm{s}^{-1}$, $0.1\ \mathrm{s}^{-1}$, and $1\ \mathrm{s}^{-1}$; each loading rate is tested by multiple times and the standard deviations are plotted in error bars. (b): The hyperelastic part $\mathbf{P}^H$ and the viscous part $\mathbf{P}^V$ of the engineering stress for different loading rates. (c): the engineering stress $\mathbf{P}_f^V$ contributed from the contour length relaxation of free chains at different loading rates. (d): the engineering stress $\mathbf{P}_c^V$ contributed from the disentanglement of free chains at different loading rates.

(Fig. 3) under the room temperature (298 K). The fitting results are verified by the relaxation test and the loading–unloading test (Fig. 4). Each test is carried out at different loading rates, and the test for each loading rate is conducted by multiple times. The fitting results are plotted in the components (11-component for uniaxial tension and 12-component for simple shear) of the engineering stress tensor $\mathbf{P}$ defined as:

$$\mathbf{P} = J\boldsymbol{\sigma}\mathbf{F}^{-T}, \tag{36}$$

with respect to the corresponding strains. The fitted material parameters are listed in Table 3. The fitting results show that the rubber modulus of the entanglement in the crosslinked network G^e is zero, indicating that almost all the entanglement comes from the free chains while the crosslinked network is almost unentangled. Such material property is also discovered from the calibration of the constitutive model on soft digital materials (DMs) [42]. The entanglement modulus G^e and G_V^e are related with the entanglement length N^e and N_V^e in the following way [25, 46]:

$$G^e = \frac{4}{5}C^R N/N^e, \tag{37a}$$

$$G_V^e = \frac{4}{5}C_V^R N_V/N_V^e. \tag{37b}$$

For a zero-valued G^e, $N^e \gg N$, which indicates that the number of the monomers between two entanglements is much larger than the number of monomers in a polymer chain in the crosslinked network. Interestingly, such results imply that the polymer chains in the crosslinked network that contributes to the hyperelasticity neither entangle with each other nor entangle with free chains. While from Eq. (37b), one can obtain the entanglement length N_V^e for the free chains' network to be approximately 54.1. It indicates that there are approximately two entanglements existing in a free chain on average. We also notice that τ_R and τ_D have the following relation [25]:

$$\tau_R/\tau_D = \frac{a}{3L}, \tag{38}$$

where L is the constant contour length of the primitive chain and a is the step length of the primitive chain. Since a is of the order of the mesh size of the network and is much smaller than L, it is reasonable that in Table 3 we have τ_R much less than τ_D.

By observing Figs. 2(a), 3(a), and 4, one can see that the fitting results is quite accurate for different loading types, as well as for a wide range of loading rates and strains. For both uniaxial tension and simple shear, the OCA shows a clear rate-dependent stress response: the faster the loading rate, the stiffer the material gets, as shown in both Figs. 2(a) and 3(a). This is because when the loading rate increases, the viscoelastic part of the stress $\mathbf{P}^V$ also increases, shown by Figs. 2(b) and 3(b). From these two figures, one can also see that the hyperelastic part contributes more than the viscous part at large strains. In Figs. 2(c) and 3(c), we plot the 11-component and 12-component for the contour length relaxation part of the viscous stress $\mathbf{P}_f^V$ and the disentanglement part $\mathbf{P}_c^V$ for the uniaxial tension test and the simple shear test, respectively. One could observe that for both the tensile test and the shear test, the contour length relaxation part $\mathbf{P}_f^V$ is almost zero at the low loading rate $\dot{\varepsilon} = 0.01\ \mathrm{s}^{-1}$. However, as the loading rate grows from $0.1\ \mathrm{s}^{-1}$ to $1\ \mathrm{s}^{-1}$, $\mathbf{P}_f^V$ increases dramatically. Since the contour length relaxation time scale τ_R is small (~ 1 s), $\mathbf{P}_f^V$ only gives significant responses at high loading rates. For the uniaxial tension test, the contour length relaxation part of the viscous

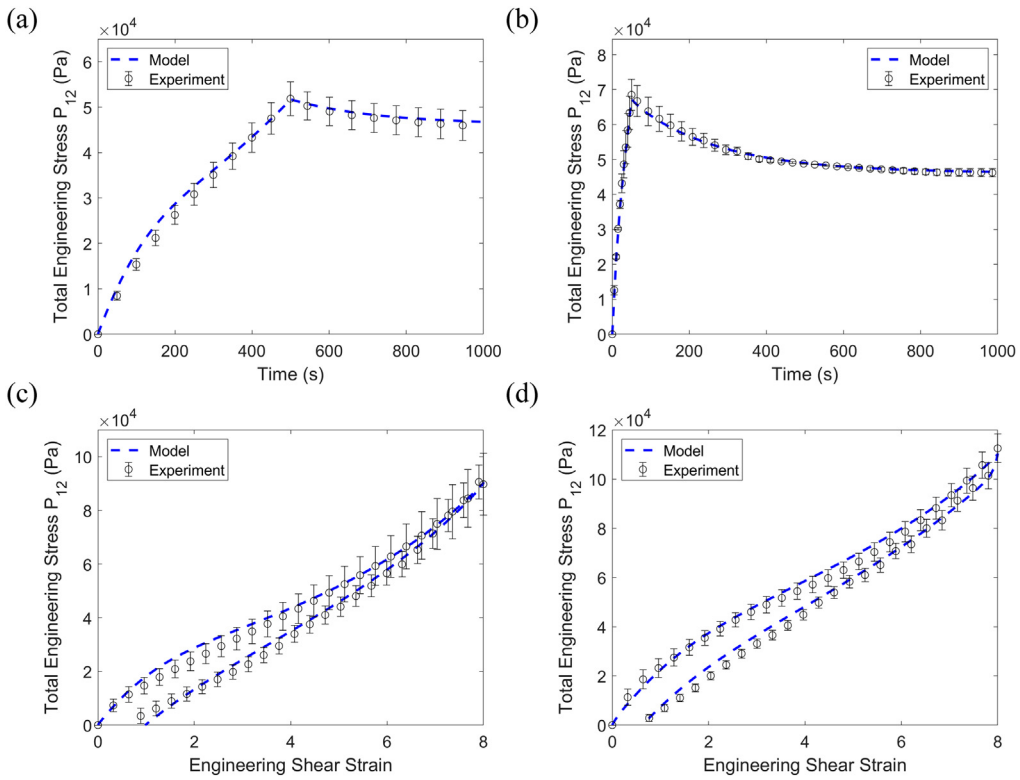

Fig. 4. The fitting results of engineering stress–time curves for the relaxation test and loading–unloading test by simple shear, compared with experiments. (a): loading rate $\dot{\varepsilon} = 0.01\ s^{-1}$, loaded up to 500% engineering shear strain. (b): loading rate $\dot{\varepsilon} = 0.1\ s^{-1}$, loaded up to 500% engineering shear strain. (c): loading/unloading rate $\dot{\varepsilon} = \pm 0.01\ s^{-1}$, loaded up to 800% engineering shear strain. (d): loading/unloading rate $\dot{\varepsilon} = \pm 0.1\ s^{-1}$, loaded up to 800% engineering shear strain.

stress $\mathbf{P}_f^V$ contributes much more to the total stress than the disentanglement part $\mathbf{P}_c^V$ at high loading rates (the green curves in Fig. 2(c) & (d)). This leads to the dramatic increase in the total engineering stress as the loading rate changes from $\dot{\varepsilon} = 0.1\ s^{-1}$ to $1\ s^{-1}$ for the uniaxial tensile test (Fig. 2(a)). For the simple shear test, the disentanglement part $\mathbf{P}_c^V$ is almost comparable to $\mathbf{P}_f^V$ at the high loading rate (the green curves in Fig. 3, (c) & (d)). And $\mathbf{P}_c^V$ increases less rapidly than $\mathbf{P}_f^V$ as the loading rate grows. Therefore, the engineering shear stress in the simple shear test increases more gently than the engineering tensile stress in the uniaxial tension test as the loading rate increases, by comparing Figs. 2(a) and 3(a).

We then testify the accuracy of our constitutive model by applying it onto the stress relaxation test and the loading–unloading test. The results plotted in Fig. 4 indicate that our constitutive model characterizes the stress relaxation response and the loading–unloading response of the OCA quite well in general. From Fig. 4(c) and (d), we could see that the stress during the unloading process is smaller than that in the loading process under the same shear strain, which implies the dissipative nature of viscoelastic materials. Moreover, we observe that a residual strain occurs when the stress reaches zero in the material: for the case $\dot{\varepsilon} = \pm 0.01\ s^{-1}$, the residual engineering shear strain is approximately 1; while for the case $\dot{\varepsilon} = \pm 0.1\ s^{-1}$, its value is roughly 0.6.

4.2. The comparison between our model with other simplified network-based constitutive models

In this part, we replace the full-network hyperelastic network response in our hyper-viscoelastic constitutive model by other simplified network-based network models to see the differences caused by these simplifications. The simplified hyperelastic models we adopt here are Khiêm and Itskov's generalized model for rubber elasticity [60] and the average-stretch model that is also known as Arruda–Boyce eight-chain model, pointed out by Beatty [18]. We note that for both models, only the network response is adopted here, while the topological constraint stress is still obtained by Eqs. (6)∼(10). The viscoelastic response in the constitutive models also remains unchanged. Firstly, we substitute the fitted material parameters in Table 3 to the new viscoelastic model with simplified hyperelastic responses and set the loading rate $\dot{\varepsilon} = 0.1\ s^{-1}$. From Fig. 5, we can see that for the same material parameters and loading rate, the full-network-based viscoelastic model gives the largest prediction, while Khiêm and Itskov's model gives the smallest prediction. This is because Khiêm and Itskov's model mainly considers the mean chain deformation with a stretch amplification exponent q according to the generalized network-averaging concept. In this model, a continuous version of Rayleigh exact distribution function is used instead of the commonly-used Langevin distribution function. And a non-affine deformation theory with the assumption that a chain may slip though entanglements ($q \leq 1$) underestimates the deformation sustained in the network chains, comparing with the average-stretch model. The non-affinity parameter q adopted in the calculation in Fig. 5 is set to be $q \approx 1$ based on Khiêm and Itskov's work on elastomers [60]. Next, we fit the material parameters by using these two simplified-network-based visco-hyperelastic constitutive models. During the fitting process, we assume that the viscoelastic response does not change, thus, τ_R and τ_D remain the same. And we further assume that the numbers of polymer chains within a unit sphere for both the crosslinked and free chains' network remain unchanged, indicating that C^R and C_V^R do not vary. If the entanglement in the crosslinked network is still negligible, then it will leave us only three material parameters: N, N_V, and G_V^e to fit, whose fitting results are listed in Table 4. The stretch amplification exponent q that relates to the deformation non-affinity is fitted as $q = 0.963$,

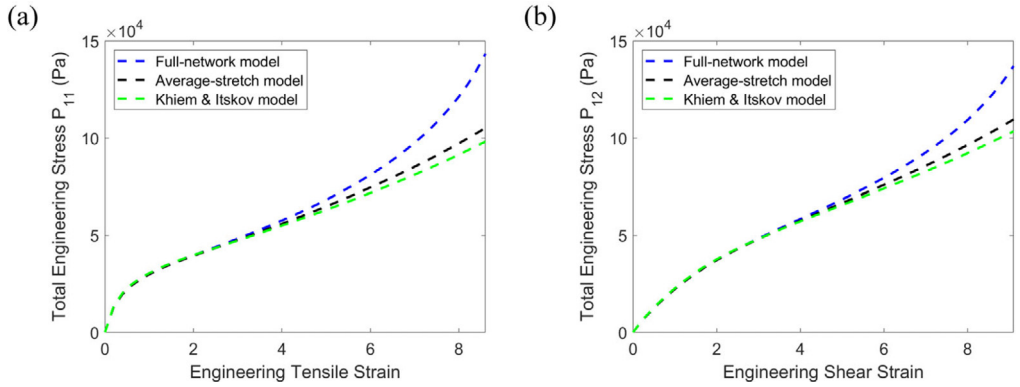

Fig. 5. Comparisons between the full-network model, the average-stretch model, and Khiêm and Itskov's generalized model for rubber elasticity. The loading rate $\dot{\varepsilon} = 0.1\ s^{-1}$. (a): the results for the uniaxial tension test. (b): the results for the simple shear test.

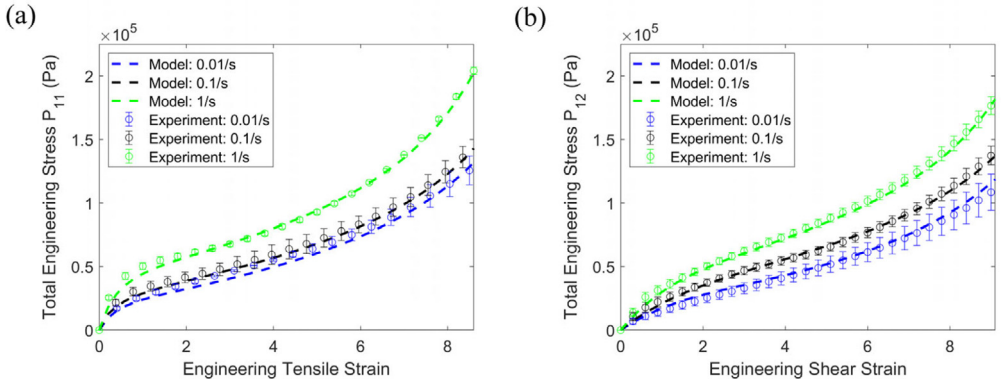

Fig. 6. The fitting results of engineering stress–strain curves by using the viscoelastic constitutive law based on Khiêm and Itskov's generalized model for rubber elasticity. (a): the experimental data and fitting results of uniaxial tension test at stretch rates $\dot{\varepsilon} = 0.01\ s^{-1}$, $0.1\ s^{-1}$, and $1\ s^{-1}$. (b): The experimental data and fitting results of uniaxial tension test at stretch rates $\dot{\varepsilon} = 0.01\ s^{-1}$, $0.1\ s^{-1}$, and $1\ s^{-1}$.

Table 2
The material parameters that need fitting.

Parameter	Physical meaning
C^R	Rubber modulus of an unentangled crosslinked network
N	The average number of the monomers of a single polymer chain in the crosslinked network
G^e	Rubber modulus of the entanglement in the crosslinked network
C_V^R	Rubber modulus of an unentangled free chains' network
N_V	The average number of the monomers of a single polymer chain in the free chains' network
G_V^e	Rubber modulus of the entanglement of free chains
τ_R	The relaxation time scale of the end-to-end contour length relaxation of free chains
τ_D	The relaxation time scale of disentanglement of free chains

indicting that an affine deformation assumption is sufficiently accurate to characterize the network deformation. The fitting curves are plotted in Figs. 6 and 7. From the both figures, we could see that both Khiêm and Itskov's model and the average-stretch-based model can give the fitting results which are as good as the full-network-based model. The difference is that Khiêm and Itskov's model underestimates the average numbers of the monomers in the crosslinked network and the free chains, as well as the entanglement modulus G_V^e of free chains more than the average-stretch-based model.

4.3. ABAQUS UMAT case study

In this part, we program the full-network-based visco-hyperelastic constitutive model into ABAQUS UMAT. Two examples: a three-point-bending simulation for a three-layered laminated plate and a uniform-curvature-bending simulation of a partially laminated plate are studied in this section to verify the applicability of our constitutive model to finite element simulations. The material parameters are adopted from Table 2.

4.3.1. The three-point-bending simulation for a three-layered laminate structure

The sample for the three-point bending simulation is a three-layered laminated plate, with the OCA being the middle layer and the PET being the upper and bottom layers. The dimensions used in the simulation are shown in Fig. 8(a). Such structure is frequently used to test the mechanical properties of OCAs in display industries [49]. The PET is modeled as a piece of isotropic linear material whose Young's modulus and the Poisson's ratio are 2.6 GPa and 0.33, [61] respectively. The Z-dimensional size of the plate is set to be much larger than the thickness so that the deformation is close to a two-dimensional case. A 1 mm-displacement load in the negative Y-direction is applied to the roller on the plate in 1 s. The distribution of the total Cauchy stress component σ_{11} around the symmetry plane (the dashed line in Fig. 8(a) & (g)) is plotted in Fig. 8(b) for $t = 1$ s. We also extract the distribution of σ_{11} along the symmetry plane with respect to the Y-coordinates at different time steps, plotted in Fig. 8(c). Since the PET is much stiffer than the OCA, the stress in PET is much larger than that in OCA. A stress discontinuity exists at the material interface due to the material inhomogeneity. From Fig. 8(c), we can see that the upper and the bottom layers of PET have their own neutral planes. The deformed configuration of the right-end of the plate is plotted at given time steps in Fig. 8(d).

Table 3
The fitted material parameters under the room temperature.

Temperature (K)	C^R (10^4 Pa)	N	G^e (10^4 Pa)	C_V^R (10^4 Pa)	N_V	G_V^e (10^4 Pa)	τ_R (s)	τ_D (s)
298	0.8556	130.4	0.0	1.8228	117.0	3.1544	0.811	227.5

Table 4
The fitted material parameters by simplified models under the room temperature.

Model	C^R (10^4 Pa)	N	G^e (10^4 Pa)	C_V^R (10^4 Pa)	N_V	G_V^e (10^4 Pa)	τ_R (s)	τ_D (s)
Khiêm and Itskov's model	0.8556	51.3	0.0	1.8228	45.2	2.6750	0.811	227.5
Average-stretch-based	0.8556	63.2	0.0	1.8228	52.0	3.0864	0.811	227.5

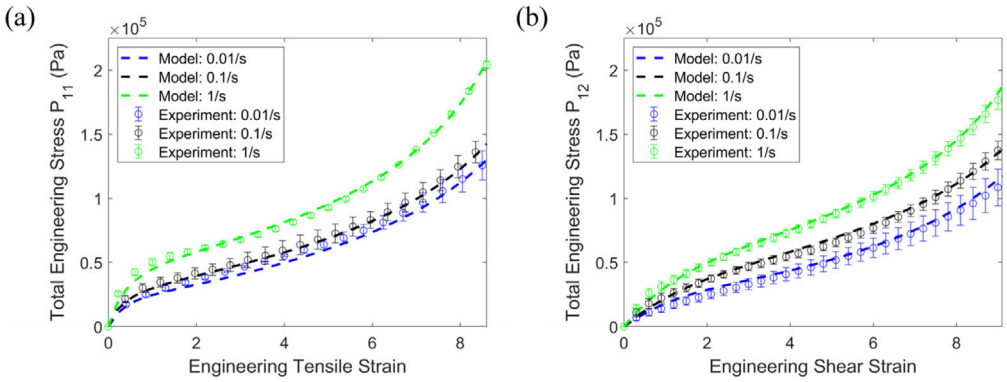

Fig. 7. The fitting results of engineering stress–strain curves by using the average-stretch-model-based viscoelastic constitutive law. (a): the experimental data and fitting results of uniaxial tension test at stretch rates $\dot{\varepsilon} = 0.01\ s^{-1}$, $0.1\ s^{-1}$, and $1\ s^{-1}$. (b): The experimental data and fitting results of uniaxial tension test at stretch rates $\dot{\varepsilon} = 0.01\ s^{-1}$, $0.1\ s^{-1}$, and $1\ s^{-1}$.

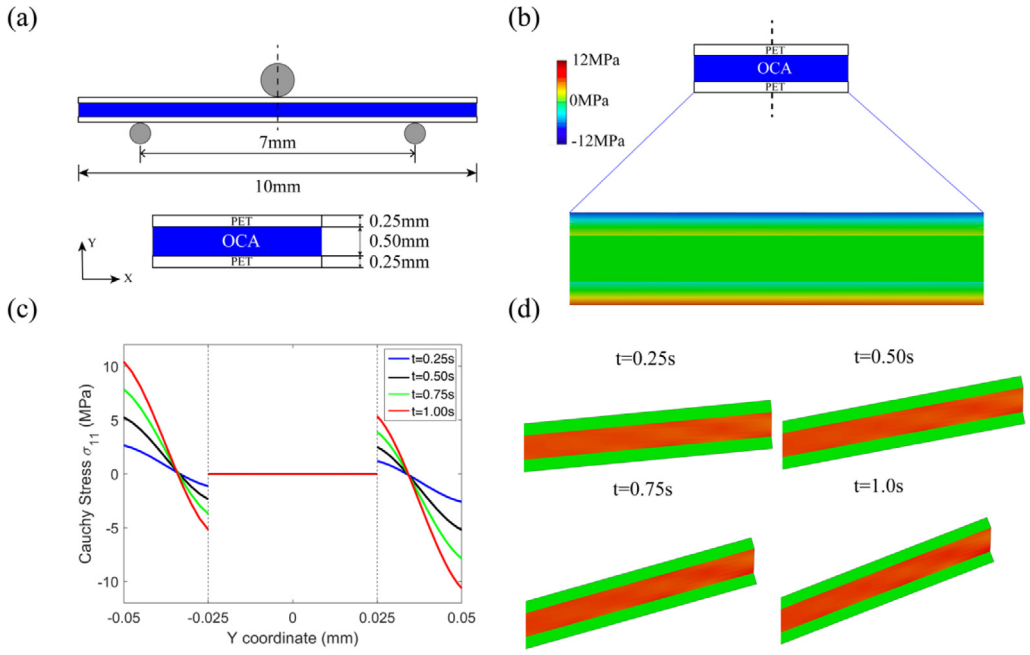

Fig. 8. A three-point-bending simulation for a three-layered laminated structure. (a) The structure and the dimensions of the composite plate. (b) The contour of σ_{11} in the laminated plate at the final time step around the symmetry plane of the structure (the dashed line). (c) The distribution of σ_{11} along the symmetry plane with respect to the Y-coordinates at different time steps. (d) The deformed configuration of the right end of the plate at given time steps. The red stands for OCA; the green stands for PET.

One could see that owing to multiple neutral planes of the PET, the intermediate OCA layer (as shown in red) is gradually sheared as the load increases.

4.3.2. The uniform-curvature-bending simulation

Next, we simulate the uniform-curvature-bending of a partially laminated plate. The plate has a middle layer made by OCA with a length equal to 15 mm. Part of the OCA, with a length of $15 - \pi r/2$ mm, is sticked to two PET plate. The dimensions of the structure are shown in Fig. 9(a). A clamped boundary constraint is applied onto the left end of the sample, shown in Fig. 9(a). In our simulation, such boundary setup is modeled as a fixed boundary condition: $\mathbf{u} = \mathbf{0}$ ($\mathbf{u}$ for the displacement vector). To make the single-layer part of the OCA bend to form an arc, we add

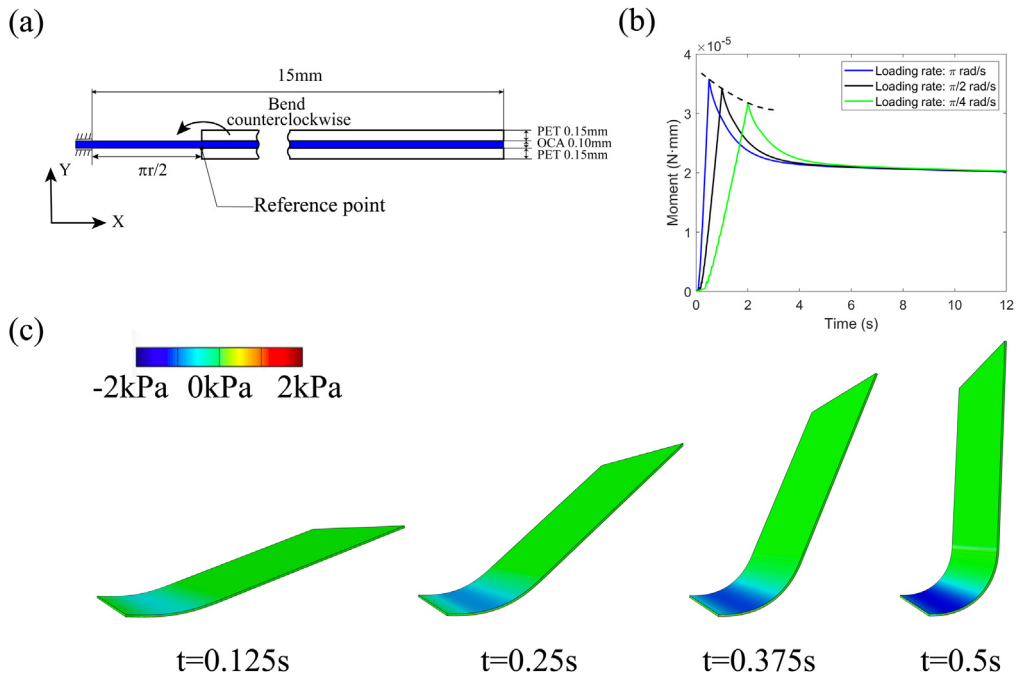

Fig. 9. A uniform-curvature-bending simulation for a partially laminated OCA-PET composite plate (a) The structure and the dimensions of the composite plate. (b) The applied moment-versus-time curve is plotted with respect to different loading time. (c) The deformed configurations and the contour of σ_{11} at different time steps, taking loading time $t_1 = 0.5$ s as an example.

a displacement and a counterclockwise rotation onto a material cross-section of the OCA layer. The material cross-section lies in the Y–Z plane with an X coordinate equal to 5 mm. In ABAQUS, it is realized by adding the displacement and the rotation load on the reference point (shown in Fig. 9(a)) which ties itself to the specified material cross-section of the OCA layer. The curvature of the neutral plane of this part of OCA remains uniform at each material point for any time step. This part of OCA will finally bend into one quarter of an entire circle at the last time step, with a radius $r = (10/\pi)$ mm, as shown in Fig. 9(c). The whole bending process is taken in $t_1 = 0.5$ s, $t_2 = 1$ s, and $t_3 = 2$ s, respectively; the structure is then hold still for another period of time. We simulate the whole process and extract the moment applied on the reference point as a function of time with respect to t_1, t_2, and t_3. The results plotted in Fig. 9(b) show that the moment applied firstly increase and then relaxes. As the loading time increases, the maximum moment decreases, shown by the dashed line.

5. Conclusions

In this paper, we propose a three-dimensional network-based visco-hyperelastic model for OCAs. This model considers both the full-network polymer structures and free polymer chains along with topological constraints due to entanglements. Two main origins of viscoelasticity: the contour length relaxation and the disentanglement of free chains are taken into consideration. The model is validated by the various of experimental tests conducted on 3M OCAs. The rate-dependent mechanical response of the model is thoroughly studied in the paper. Later, we replace the full-network hyperelastic response applied in our constitutive model by other simplified physical models to see the differences caused by the simplifications. We find that both Khiêm and Itskov's model and the average-stretch-based model underestimate not only the average numbers of the monomers in the crosslinked and the free chains' network, but also the entanglement modulus G_V^e of free chains. Additionally, we have proposed a material update scheme for ABAQUS UMAT. Two finite element implementations of our constitutive model are presented in the last part of the work.

Declaration of competing interest

The authors declare that they have no known competing financial interests or personal relationships that could have appeared to influence the work reported in this paper.

Acknowledgments

T.Z., B.X., and H.Y. acknowledge the funding support from the National Natural Science Foundation of China (NSFC Grant No. 12072143) and Guangdong OPPO Mobile Telecommunication Co. Ltd, China.

References

[1] C.J. Campbell, Optically clear adhesives, in: J. Chen, W. Cranton, M. Fihn (Eds.), In Handbook of Visual Display Technology, Springer International Publishing, Cham, 2016, pp. 1501–1514, http://dx.doi.org/10.1007/978-3-319-14346-0_197.

[2] S.D. Tobing, A. Klein, Molecular parameters and their relation to the adhesive performance of acrylic pressure-sensitive adhesives, J. Appl. Polym. Sci. 79 (2001) 2230–2244.

[3] S.D. Tobing, A. Klein, Molecular parameters and their relation to the adhesive performance of emulsion acrylic pressure-sensitive adhesives. II. Effect of crosslinking, J. Appl. Polym. Sci. 79 (2001) 2558–2564.

[4] A. Lindner, B. Lestriez, S. Mariot, C. Creton, T. Maevis, B. Lühmann, R. Brummer, Adhesive and rheological properties of lightly crosslinked model acrylic networks, J. Adhes. 82 (3) (2006) 267–310, http://dx.doi.org/10.1080/00218460600646594.

[5] C. Creton, G. Hu, F. Deplace, L. Morgret, K.R. Shull, Large-strain mechanical behavior of model block copolymer adhesives, Macromolecules 42 (20) (2009) 7605–7615, http://dx.doi.org/10.1021/ma900821k.

[6] K.S. Cho, Viscoelasticity of polymers, in: Springer Series in Materials Science, Springer Netherlands, Dordrecht, 2016, p. 241, http://dx.doi.org/10.1007/978-94-017-7564-9.

[7] Y. Jia, Z. Liu, D. Wu, J. Chen, H. Meng, Mechanical simulation of foldable AMOLED panel with a module structure, Org. Electron. 65 (2019) 185–192, http://dx.doi.org/10.1016/j.orgel.2018.11.026.

[8] R.S. Rivlin, D.W. Saunders, Large elastic deformations of isotropic materials VII. Experiments on the deformation of rubber, Philos. Trans. R. Soc. Lond. Ser. Math. Phys. Sci. 243 (865) (1951) 251–288, http://dx.doi.org/10.1098/rsta.1951.0004.

[9] L.J. Hart-Smith, Elasticity parameters for finite deformations of rubber-like materials, Z. Für Angew. Math. Phys. ZAMP 17 (5) (1966) 608–626, http://dx.doi.org/10.1007/BF01597242.
[10] R.W. Ogden, Large deformation isotropic elasticity – on the correlation of theory and experiment for incompressible rubberlike solids, Proc. R. Soc. Lond. Ser. Math. Phys. Eng. Sci. 326 (1972) 565–584.
[11] O.H. Yeoh, Characterization of elastic properties of carbon-black-filled rubber vulcanizates, Rubber. Chem. Technol. 63 (1990) 792–805.
[12] H. Khajehsaeid, J. Arghavani, R. Naghdabadi, A hyperelastic constitutive model for rubber-like materials, Eur. J. Mech. ASolids 38 (2013) 144–151, http://dx.doi.org/10.1016/j.euromechsol.2012.09.010.
[13] R.L. Jernigan, P.J. Flory, Distribution functions for chain molecules, J. Chem. Phys. 50 (10) (1969) 4185–4200, http://dx.doi.org/10.1063/1.1670884.
[14] W. Kuhn, F. Grün, Statistical behavior of the single chain molecule and its relation to the statistical behavior of assemblies consisting of many chain molecules, J. Polym. Sci. 1 (3) (1946) 183–199, http://dx.doi.org/10.1002/pol.1946.120010306.
[15] W. Kuhn, F. Grün, Beziehungen zwischen elastischen Konstanten und Dehnungsdoppelbrechung hochelastischer Stoffe, Kolloid-Z. 101 (3) (1942) 248–271, http://dx.doi.org/10.1007/BF01793684.
[16] H.M. James, E. Guth, Theory of the elastic properties of rubber, J. Chem. Phys. 11 (10) (1943) 455–481, http://dx.doi.org/10.1063/1.1723785.
[17] E.M. Arruda, M.C. Boyce, A three-dimensional constitutive model for the large stretch behavior of rubber elastic materials, J. Mech. Phys. Solids 41 (2) (1993) 389–412, http://dx.doi.org/10.1016/0022-5096(93)90013-6.
[18] M.F. Beatty, An average-stretch full-network model for rubber elasticity, J. Elasticity 70 (2003) 65–86.
[19] P.D. Wu, E. Van Der Giessen, On improved network models for rubber elasticity and their applications to orientation hardening in glassy polymers, J. Mech. Phys. Solids 41 (3) (1993) 427–456, http://dx.doi.org/10.1016/0022-5096(93)90043-F.
[20] C. Miehe, S. Göktepe, F. Lulei, A micro-macro approach to rubber-like materials. Part I: The non-affine micro-sphere model of rubber elasticity, J. Mech. Phys. Solids 52 (11) (2004) 2617–2660, http://dx.doi.org/10.1016/j.jmps.2004.03.011.
[21] T.C.B. McLeish, Tube theory of entangled polymer dynamics, Adv. Phys. 51 (6) (2002) 1379–1527.
[22] R.T. Deam, S.F. Edwards, The theory of rubber elasticity, Philos. Trans. R. Soc. Lond. Ser. A 280 (1976) 317–353.
[23] S.F. Edwards, T.A. Vilgis, The tube model theory of rubber elasticity, Rep. Progr. Phys. 51 (2) (1988) 243–297, http://dx.doi.org/10.1088/0034-4885/51/2/003.
[24] M. Doi, S.F. Edwards, Dynamics of concentrated polymer systems. Part 1.—Brownian motion in the equilibrium state, J. Chem. Soc. Faraday. Trans. 2 (74) (1978) 1789–1801, http://dx.doi.org/10.1039/F29787401789.
[25] M. Doi, S.F. Edwards, He Theory of Polymer Dynamics, Oxford University Press Inc., New York, 1986.
[26] G. Heinrich, E. Straube, On the strength and deformationdependence of the tube-like topological constraints of polymer networks, melts and concentrated solutions, Acta Polym. 34 (9) (1983) 589–594, http://dx.doi.org/10.1002/actp.1983.010340909.
[27] G. Heinrich, E. Straube, On the strength and deformation dependence of the tube-like topological constraints of polymer networks, melts and concentrated solutions. II. Polymer melts and concentrated solutions, Acta Polym. 35 (2) (1984) 115–119, http://dx.doi.org/10.1002/actp.1984.010350201.
[28] G. Heinrich, M. Kaliske, Theoretical and numerical formulation of a molecular based constitutive tube-model of rubber elasticity, Comput. Theor. Polym. Sci. 7 (3–4) (1997) 227–241, http://dx.doi.org/10.1016/S1089-3156(98)00010-5.
[29] G. Heinrich, E. Straube, G. Helmis, Rubber elasticity of polymer networks: Theories, in: Polymer Physics, Springer Berlin Heidelberg, Berlin, Heidelberg, 1988, pp. 33–87.
[30] B. Meissner, L. Matějka, A Langevin-elasticity-theory-based constitutive equation for rubberlike networks and its comparison with biaxial stress–strain data. Part I, Polymer 44 (16) (2003) 4599–4610, http://dx.doi.org/10.1016/S0032-3861(03)00411-7.
[31] Y. Xiang, D. Zhong, P. Wang, G. Mao, H. Yu, S. Qu, A general constitutive model of soft elastomers, J. Mech. Phys. Solids 117 (2018) 110–122, http://dx.doi.org/10.1016/j.jmps.2018.04.016.
[32] J.C. Simo, On a fully three-dimensional finite-strain viscoelastic damage model: Formulation and computational aspects, Comput. Methods Appl. Mech. Engrg. 60 (2) (1987) 153–173, doi:10/bkb5bs.
[33] G.A. Holzapfel, On large strain viscoelasticity: continuum formulation and finite element applications to elastomeric structures, Internat. J. Numer. Methods Engrg. 39 (1996) 3903–3926.
[34] A. Lion, A constitutive model for carbon black filled rubber: Experimental investigations and mathematical representation, Contin. Mech. Thermodyn. 8 (3) (1996) 153–169, http://dx.doi.org/10.1007/BF01181853.
[35] S. Reese, S. Govindjee, A theory of finite viscoelasticity and numerical aspects, Int. J. Solids Struct. 35 (26–27) (1998) 3455–3482, http://dx.doi.org/10.1016/S0020-7683(97)00217-5.
[36] J.S. Bergström, M.C. Boyce, Constitutive modeling of the time-dependent and cyclic loading of elastomers and application to soft biological tissues, Mech. Mater. 33 (9) (2001) 523–530, http://dx.doi.org/10.1016/S0167-6636(01)00070-9.
[37] C. Miehe, S. Göktepe, A micro–macro approach to rubber-like materials. Part II: The micro-sphere model of finite rubber viscoelasticity, J. Mech. Phys. Solids 53 (10) (2005) 2231–2258, http://dx.doi.org/10.1016/j.jmps.2005.04.006.
[38] H. Khajehsaeid, J. Arghavani, R. Naghdabadi, S. Sohrabpour, A visco-hyperelastic constitutive model for rubber-like materials: A rate-dependent relaxation time scheme, Internat. J. Engrg. Sci. 79 (2014) 44–58, http://dx.doi.org/10.1016/j.ijengsci.2014.03.001.
[39] J. Liu, M. Latorre, A.L. Marsden, A continuum and computational framework for viscoelastodynamics: I. Finite deformation linear models, Comput. Methods Appl. Mech. Engrg. 385 (2021) 114059, http://dx.doi.org/10.1016/j.cma.2021.114059.
[40] M. Doi, S.F. Edwards, Dynamics of concentrated polymer systems. Part 2.—Molecular motion under flow, J. Chem. Soc. Faraday Trans. 2 (74) (1978) 1802–1817, http://dx.doi.org/10.1039/F29787401802.
[41] Y.-H. Lin, Polymer viscoelasticity: Basics, molecular theories, experiments and simulations, in: World Scientific, second ed., 2010, http://dx.doi.org/10.1142/7786.
[42] Y. Xiang, D. Zhong, P. Wang, T. Yin, H. Zhou, H. Yu, C. Baliga, S. Qu, W. Yang, A physically based visco-hyperelastic constitutive model for soft materials, J. Mech. Phys. Solids 128 (2019) 208–218, http://dx.doi.org/10.1016/j.jmps.2019.04.010.
[43] R.J. Clifton, X. Wang, T. Jiao, A physically-based, quasilinear viscoelasticity model for the dynamic response of polyurea, J. Mech. Phys. Solids 93 (2016) 8–15, http://dx.doi.org/10.1016/j.jmps.2016.04.027.
[44] S. Tang, M. Steven Greene, W.K. Liu, Two-scale mechanism-based theory of nonlinear viscoelasticity, J. Mech. Phys. Solids 60 (2) (2012) 199–226, http://dx.doi.org/10.1016/j.jmps.2011.11.003.
[45] Y. Li, S. Tang, B.C. Abberton, M. Kröger, C. Burkhart, B. Jiang, G.J. Papakonstantopoulos, M. Poldneff, W.K. Liu, A predictive multiscale computational framework for viscoelastic properties of linear polymers, Polymer 53 (25) (2012) 5935–5952, http://dx.doi.org/10.1016/j.polymer.2012.09.055.
[46] Ying Li, S. Tang, M. Kröger, Wing Kam Liu, Molecular simulation guided constitutive modeling on finite strain viscoelasticity of elastomers, J. Mech. Phys. Solids 88 (2016) 204–226, http://dx.doi.org/10.1016/j.jmps.2015.12.007.
[47] A. Cheng, Q. Wei, J. Jin, T. Su, D. Peng, 84-2: Study on reliability for impact and rolling of film stacks in Rollable AMOLED display by finite element analysis, SID Symp. Dig. Tech. Pap. 51 (1) (2020) 1265–1268, http://dx.doi.org/10.1002/sdtp.14110.
[48] F. Salmon, A. Everaerts, C. Campbell, B. Pennington, B. Erdogan-Haug, G. Caldwell, 64-1: Modeling the mechanical performance of a foldable display panel bonded by 3M optically clear adhesives, SID Symp. Dig. Tech. Pap. 48 (1) (2017) 938–941.
[49] M.M. Nath, G. Gupta, Modeling the mechanical performance of bendable display under cyclic loading, in: 2019 IEEE International Flexible Electronics Technology Conference (IFETC), IEEE, Vancouver, BC, Canada, 2019, pp. 1–5, http://dx.doi.org/10.1109/IFETC46817.2019.9073716.
[50] M. Wang, D. Chen, W. Feng, A. Zhong, Synthesis and characterization of optically clear pressure-sensitive adhesive, Mater. Trans. 56 (6) (2015) 895–898, http://dx.doi.org/10.2320/matertrans.M2014425.
[51] M. Rubinstein, S. Panyukov, Nonaffine deformation and elasticity of polymer networks, Macromolecules 30 (25) (1997) 8036–8044, http://dx.doi.org/10.1021/ma970364k.
[52] M. Rubinstein, S. Panyukov, Elasticity of polymer networks, Macromolecules 35 (17) (2002) 6670–6686, http://dx.doi.org/10.1021/ma0203849.
[53] J.D. Davidson, N.C. Goulbourne, A nonaffine network model for elastomers undergoing finite deformations, J. Mech. Phys. Solids 61 (8) (2013) 1784–1797, http://dx.doi.org/10.1016/j.jmps.2013.03.009.
[54] E. Darabi, M. Itskov, A generalized tube model of rubber elasticity, Soft Matter 17 (6) (2021) 1675–1684, http://dx.doi.org/10.1039/D0SM02055A.
[55] A. Wineman, Nonlinear viscoelastic solids—A review, Math. Mech. Solids 14 (3) (2009) 300–366, http://dx.doi.org/10.1177/1081286509103660.
[56] V. Slesarenko, S. Rudykh, Towards mechanical characterization of soft digital materials for multimaterial 3D-printing, Internat. J. Engrg. Sci. 123 (2018) 62–72, http://dx.doi.org/10.1016/j.ijengsci.2017.11.011.
[57] O. Chaudhuri, J. Cooper-White, P.A. Janmey, D.J. Mooney, V.B. Shenoy, Effects of extracellular matrix viscoelasticity on cellular behaviour, Nature 584 (7822) (2020) 535–546, http://dx.doi.org/10.1038/s41586-020-2612-2.
[58] S.J. Connolly, D. Mackenzie, Y. Gorash, Isotropic hyperelasticity in principal stretches: Explicit elasticity tensors and numerical implementation, Comput. Mech. 64 (5) (2019) 1273–1288, http://dx.doi.org/10.1007/s00466-019-01707-1.

[59] J.A. Nelder, R. Mead, A simplex method for function minimization, Comput. J. 7 (4) (1965) 308–313.
[60] V.N. Khiêm, M. Itskov, Analytical network-averaging of the tube model, J. Mech. Phys. Solids 95 (2016) 254–269, http://dx.doi.org/10.1016/j.jmps.2016.05.030.
[61] Y. Bin, K. Oishi, K. Yoshida, M. Matsuo, Mechanical properties of poly(ethylene terephthalate) estimated in terms of orientation distribution of crystallites and amorphous chain segments under simultaneous biaxially stretching, Polym. J. 36 (11) (2004) 888–898, http://dx.doi.org/10.1295/polymj.36.888.